

A Two-Dimensional Third-Order CESE Scheme for Ideal MHD Equations

Yufen Zhou^{1,*} and Xueshang Feng^{1,2}

¹ SIGMA Weather Group, State Key Laboratory for Space Weather, National Space Science Center, Chinese Academy of Science, Beijing 100190, China.

² Shenzhen Key Laboratory of Numerical Prediction for Space Storm, Institute of Space Science and Applied Technology, Harbin Institute of Technology, Shenzhen 518055, China.

Received 21 October 2022; Accepted (in revised version) 23 May 2023

Abstract. In this paper, we construct a two-dimensional third-order space-time conservation element and solution element (CESE) method and apply it to the magnetohydrodynamics (MHD) equations. This third-order CESE method preserves all the favorable attributes of the original second-order CESE method, such as: (i) flux conservation in space and time without using an approximated Riemann solver, (ii) genuine multi-dimensional algorithm without dimensional splitting, (iii) the use of the most compact mesh stencil, involving only the immediate neighboring cells surrounding the cell where the solution at a new time step is sought, and (iv) an explicit, unified space-time integration procedure without using a quadrature integration procedure. In order to verify the accuracy and efficiency of the scheme, several 2D MHD test problems are presented. The result of MHD smooth wave problem shows third-order convergence of the scheme. The results of the other MHD test problems show that the method can enhance the solution quality by comparing with the original second-order CESE scheme.

AMS subject classifications: 65M08, 76W05

Key words: CESE method, third-order, MHD equations.

1 Introduction

The space-time conservation element and solution element (CESE) method was originally proposed by Chang and co-workers [6,7] for solving conservation laws. In contrast to conventional finite volume method (FVM) and finite difference method (FDM), the CESE method has several unique features. It treats space and time in a unified manner

*Corresponding author. *Email addresses:* yfzhou@swl.ac.cn (Y. Zhou), fengx@swl.ac.cn (X. Feng)

when imposing local and global space-time flux conservation. There is no need to employ the reconstruction or Riemann solver. The space-time domain is divided into space-time Solution Elements (SEs), in which the primary unknowns and the fluxes are discretized and represented by simple smooth functions. The space-time domain is also divided into non-overlapping space-time Conservation Elements (CEs), over which flux conservation is enforced in both space and time. It has the most compact stencil. Only the immediate neighboring mesh cells of the solution point are involved in the computational algorithm. It achieves the same accuracy in time and space with a fully discrete one-stage formulation. Owing to its numerical accuracy and robustness, the CESE method has been successfully extended and applied to compute Euler, e.g., [3, 4, 36], Navier-Stokes, e.g., [10, 15, 27], and magnetohydrodynamic (MHD) equations, e.g., [13, 14, 22, 33].

However, the original CESE scheme [6, 7] cannot be directly applied in the viscous flow and inviscid flow problems with shocks due to its non-dissipative property. To overcome the shortcoming, Zhang *et al.* [36] proposed its dissipative extension for solving the unsteady Euler equations. But it is sensitive to the local Courant Friedrichs Lewy (CFL) number. To overcome this limitation, a Courant number insensitive (CNI) CESE scheme is proposed to adjust the dissipation via the local CFL number [8, 30, 34, 35]. Later, by introducing approximate Riemann solvers or other upwind techniques to compute the flux vector at the interfaces between sub-CEs, Shen *et al.* [24, 26] and Shen and Wen [25] proposed upwind CESE schemes for capturing contact discontinuities. Efforts have also been made to design higher-order CESE schemes. Liu and Wang [20] developed an arbitrary-order one-dimensional CESE scheme based on arbitrary Taylor expansions in the solution elements. Chang [9] proposed a highly-stable high-order CESE method for solving the one-dimensional Burgers equation. Then Bilyeu *et al.* [3, 4] extended Chang's work to solve a system of linear and non-linear hyperbolic partial differential equations in one- and two-dimensions. Shen *et al.* [23] extended it to high-order versions including third and fourth order for the Euler equation on hybrid grids in two-dimensions. Yang *et al.* [33] extended the CESE MHD solver to a fourth-order version. However, the fourth-order CESE MHD solver can only be applied to the rectangular grids in Cartesian coordinate. All the boundaries of the CEs are parallel to the coordinate surfaces, and the normal direction is along the coordinate axis.

Moreover, so far, there is no detailed derivation of the third-order accuracy CESE method for MHD equations. In the present study, we extend the second-order CESE method to third orders for 2D MHD equations and report detailed derivation. Moreover, the third-order CESE scheme can be directly applied to the unstructured meshes. The third-order CESE method preserves all the features of the original second-order CESE method. It can provide more accurate solutions. For testing the accuracy, resolution, and efficiency of the third-order CESE method, we simulate several 2D MHD benchmark problems, such as smooth Alfvén wave problem, oblique shock tube problem, Orszag-Tang vortex and rotor problem.

The paper is organized as follows. Section 2 illustrates the 2D MHD governing equations. Section 3 presents the CESE method for calculating the flow variables. Section 4

presents the method for calculating the spatial derivatives. Numerical examples are carried out to demonstrate the accuracy and robustness of the present scheme in Section 5. Conclusions are given in Section 6.

2 MHD governing equations

The ideal MHD equations include the continuity, the momentum, the energy, and the magnetic induction equations [12, 19, 32]. The two dimensional ideal MHD equations in conservative form are as follows:

$$\frac{\partial \mathbf{U}}{\partial t} + \frac{\partial \mathbf{F}(\mathbf{U})}{\partial x} + \frac{\partial \mathbf{G}(\mathbf{U})}{\partial y} = 0, \quad (2.1)$$

where $\mathbf{U} = (\rho, \rho u, \rho v, \rho w, e, B_x, B_y, B_z)^T = (u_1, u_2, u_3, u_4, u_5, u_6, u_7, u_8)^T$ is the state vector of the conservative variables.

$$\mathbf{F}(\mathbf{U}) = \begin{pmatrix} \rho u \\ \rho u^2 + p_0 - B_x^2 \\ \rho uv - B_x B_y \\ \rho uw - B_x B_z \\ (e + p_0)u - B_x(uB_x + vB_y + wB_z) \\ 0 \\ uB_y - vB_x \\ uB_z - wB_x \end{pmatrix} = (f_1, f_2, f_3, f_4, f_5, f_6, f_7, f_8)^T$$

and

$$\mathbf{G}(\mathbf{U}) = \begin{pmatrix} \rho v \\ \rho vu - B_y B_x \\ \rho v^2 + p_0 - B_y^2 \\ \rho vw - B_y B_z \\ (e + p_0)v - B_y(uB_x + vB_y + wB_z) \\ vB_x - uB_y \\ 0 \\ vB_z - wB_y \end{pmatrix} = (g_1, g_2, g_3, g_4, g_5, g_6, g_7, g_8)^T.$$

Here, ρ and p are mass density and gas pressure, respectively; $\mathbf{u} = (u, v, w)$ and $\mathbf{B} = (B_x, B_y, B_z)$ denote velocity and magnetic field, respectively. The total energy e is $e = p/(\gamma - 1) + \rho(u^2 + v^2 + w^2)/2 + (B_x^2 + B_y^2 + B_z^2)/2$ and the total pressure is $p_0 = p + (B_x^2 + B_y^2 + B_z^2)/2$.

3 Third-order CESE method

In this section, we will illustrate the third-order CESE method in 2D space. For the sake of conciseness, we present the CESE method based on a uniform quadrilateral meshes.

The third-order CESE scheme can be directly applied to the unstructured meshes.

3.1 Definitions of CE and SE

Conservation Elements (CEs) are the non-overlapping space-time regions, which cover the whole space-time domain. Flux conservation is enforced over each of them. Solution elements are also space-time sub-domains, over which any physical flux vector is approximated using simple smooth functions. In the original CESE scheme, the solution is only updated at the cell centers. Later, Wang *et al.* [31] designed a new type of SE and CE. They alternatively updated the solution between the cell centers and cell vertices. In this paper, the geometry of CE and SE in the third-order CESE method follows that of the original two-dimensional CESE method [36]. It is already considered in the previous Euler/Navier-Stokes case [6, 10, 36]. For completeness, a brief illustration is provided.

We firstly divide the x - y plane into non-overlapping uniform quadrilaterals and any two neighboring quadrilaterals share a common side (see Fig. 1). The centroids of quadrilaterals are marked by hollow circles or solid circles. If the centroid of a quadrilateral is marked by a solid (hollow) circle, the centroids of the four neighboring quadrilaterals are marked by hollow (solid) circles.

In Fig. 1, point Q , centroid of a typical quadrilateral $B_1B_2B_3B_4$, is marked by a solid circle, while the points A_ℓ , $\ell = 1, 2, 3, 4$, respectively, are the centroids of the four quadrilaterals neighboring to the quadrilateral $B_1B_2B_3B_4$ and are marked by hollow circles. Solution point Q^* is defined at the centroid of $A_1B_1A_2B_2A_3B_3A_4B_4$. In general, the centroid does not coincide with the solution point in a mesh cell, namely, for example, points Q and Q^* of quadrilateral $B_1B_2B_3B_4$ may not coincide. Moreover, the solution points are where time-marching solutions are calculated and stored. Let n be index for t . Points A_ℓ , B_ℓ , Q and Q^* are at the time level n . A'_ℓ , B'_ℓ , Q' and Q'^* are at the time level $n-1/2$. A''_ℓ , B''_ℓ , Q'' and Q''^* are at the time level $n+1/2$.

As shown in Fig. 2(a), the SE of point Q is the union of the five plane segments $B'_1Q'Q''B''_1$, $B'_2Q'Q''B''_2$, $B'_3Q'Q''B''_3$, $B'_4Q'Q''B''_4$, and $A_1B_1A_2B_2A_3B_3A_4B_4$. The geometry of the four conservation elements (CEs) associated with point Q is shown in

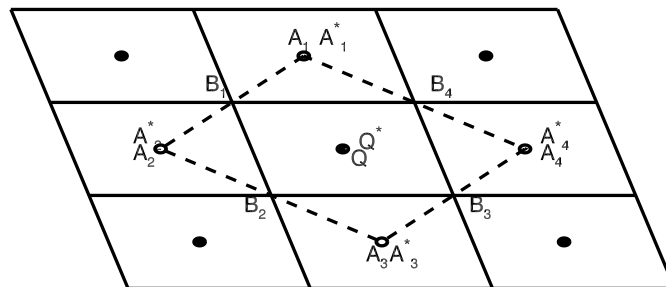


Figure 1: Space mesh in an x - y plane.

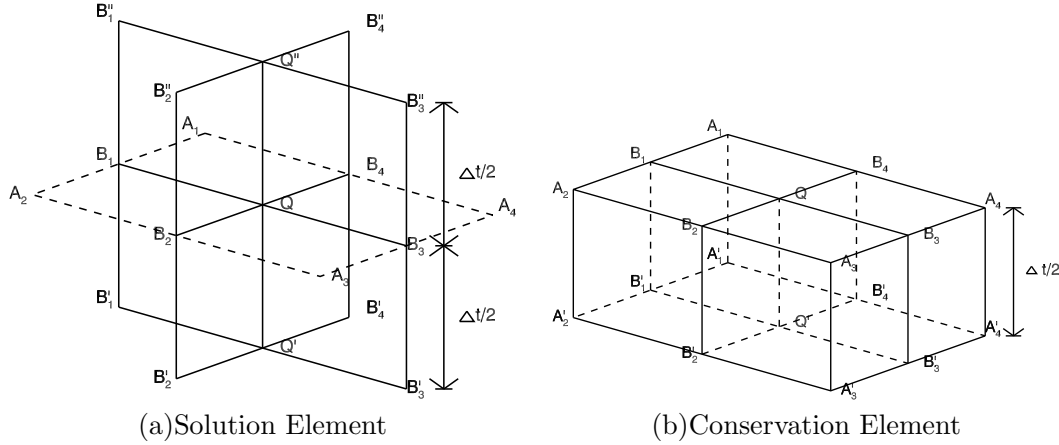


Figure 2: The definitions of CE and SE associated with point Q .

Fig. 2(b). The four CEs are rectangular cylinders defined by points $A'_1B'_1Q'B'_4A_1B_1QB_4$, $A'_2B'_2Q'B'_1A_2B_2QB_1$, $A'_3B'_3Q'B'_2A_3B_3QB_2$ and $A'_4B'_4Q'B'_3A_4B_4QB_3$. In each CE there are 6 rectangular surfaces. Three of them are part of the SE associated with point Q^* . The other three are associated with the solution points at the previous time step. For example the CE defined by points $A'_1B'_1Q'B'_4A_1B_1QB_4$ has three rectangular surfaces associated with point Q^* : $B'_1Q'QB_1$, $B'_4Q'QB_4$ and $A_1B_1QB_4$. The other three rectangular surfaces $A'_1B'_1B_1A_1$, $A'_4B'_4B_4A_4$ and $A'_1B'_1Q'B'_4$ are a part of the SE associated with point A_1^* .

The union of the four CEs associated with point Q^* forms a Composite CE (CCE), which is the hexahedron $A_1B_1A_2B_2A_3B_3A_4B_4A'_1B'_1A'_2B'_2A'_3B'_3A'_4B'_4$ as shown in Fig. 2(b). When combining the four CEs to form the CCE, fluxes passing the four interfaces between the neighboring CEs, $B'_1Q'QB_1$, $B'_2Q'QB_2$, $B'_3Q'QB_3$ and $B'_4Q'QB_4$, cancel each other. Therefore, if the space-time flux conservation is satisfied in each of the four CEs, it would be satisfied over the CCE. Moreover, the solution point Q^* is the centroid of the top surface of the CCE defined by points $A_1B_1A_2B_2A_3B_3A_4B_4$.

3.2 Approximations within a solution element

Following Chang's original approach [6], inside each SE the flow variables and the fluxes are assumed smooth, and are represented by the second-order Taylor expansion in space and time. For any $(x, y, t) \in SE(Q^*)$, $u_m^*(x, y, t)$, $f_m^*(x, y, t)$, and $g_m^*(x, y, t)$, respectively, are approximated by:

$$\begin{aligned}
 u_m^*(x, y, t) = & (u_m)_{Q^*} + (u_{mx})_{Q^*} \Delta x + (u_{my})_{Q^*} \Delta y + (u_{mt})_{Q^*} \Delta t \\
 & + \frac{1}{2} \{ (u_{mxx})_{Q^*} \Delta x^2 + (u_{myy})_{Q^*} \Delta y^2 + (u_{mtt})_{Q^*} \Delta t^2 + [(u_{mxy})_{Q^*} + (u_{myx})_{Q^*}] \Delta x \Delta y \} \\
 & + (u_{mxt})_{Q^*} \Delta x \Delta t + (u_{myt})_{Q^*} \Delta y \Delta t,
 \end{aligned} \tag{3.1a}$$

$$\begin{aligned}
 f_m^*(x,y,t) &= (f_m)_{Q^*} + (f_{mx})_{Q^*} \Delta x + (f_{my})_{Q^*} \Delta y + (f_{mt})_{Q^*} \Delta t \\
 &\quad + \frac{1}{2} \{ (f_{mxx})_{Q^*} \Delta x^2 + (f_{myy})_{Q^*} \Delta y^2 + (f_{mtt})_{Q^*} \Delta t^2 + [(f_{mxy})_{Q^*} + (f_{myx})_{Q^*}] \Delta x \Delta y \} \\
 &\quad + (f_{mxt})_{Q^*} \Delta x \Delta t + (f_{myt})_{Q^*} \Delta y \Delta t,
 \end{aligned} \tag{3.1b}$$

$$\begin{aligned}
 g_m^*(x,y,t) &= (g_m)_{Q^*} + (g_{mx})_{Q^*} \Delta x + (g_{my})_{Q^*} \Delta y + (g_{mt})_{Q^*} \Delta t \\
 &\quad + \frac{1}{2} \{ (g_{mxx})_{Q^*} \Delta x^2 + (g_{myy})_{Q^*} \Delta y^2 + (g_{mtt})_{Q^*} \Delta t^2 + [(g_{mxy})_{Q^*} + (g_{myx})_{Q^*}] \Delta x \Delta y \} \\
 &\quad + (g_{mxt})_{Q^*} \Delta x \Delta t + (g_{myt})_{Q^*} \Delta y \Delta t,
 \end{aligned} \tag{3.1c}$$

where $\Delta x = x - x_Q^*$, $\Delta y = y - y_Q^*$ and $\Delta t = t - t^n$. x_Q^* , y_Q^* and t^n are the space-time coordinates of point Q^* .

By using the chain rule, all the derivatives of flux f and g with respect to x , y and t can be obtained as follows:

$$\frac{\partial T_m}{\partial \phi_1} = \sum_{p=1}^8 \frac{\partial T_m}{\partial u_p} \frac{\partial u_p}{\partial \phi_1}, \tag{3.2a}$$

$$\frac{\partial^2 T_m}{\partial \phi_1 \partial \phi_2} = \sum_{p=1}^8 \frac{\partial T_m}{\partial u_p} \frac{\partial^2 u_p}{\partial \phi_1 \partial \phi_2} + \sum_{p=1}^8 \sum_{q=1}^8 \frac{\partial^2 T_m}{\partial u_p \partial u_q} \frac{\partial u_p}{\partial \phi_1} \frac{\partial u_q}{\partial \phi_2}, \tag{3.2b}$$

where T_m represents f_m or g_m , and $(\phi_1, \phi_2) = \{(x,x), (y,y), (t,t), (x,y), (y,x), (x,t), (y,t)\}$. $\frac{\partial T_m}{\partial u_p}, \frac{\partial^2 T_m}{\partial u_p \partial u_q}$ are the elements of the Jacobian matrices. The Jacobian matrices can be obtained by directly taking the derivative of flux with respect to every conservative variable in sequence.

According to Eq. (3.2a), we can obtain f_{mx} and g_{my} . By using the Cauchy-Kovalewski procedure for non linear equations [11, 12], according to the conservation law expressed by Eq. (2.1), we have

$$u_{mt} = -f_{mx} - g_{my}. \tag{3.3}$$

Then, we apply $\partial/\partial x, \partial/\partial y$ and $\partial/\partial t$ to Eq. (3.3) to have

$$u_{mxt} = -f_{mxx} - g_{myx}, \tag{3.4a}$$

$$u_{myt} = -f_{mxy} - g_{myy}, \tag{3.4b}$$

$$u_{mtt} = -f_{mxt} - g_{myt}, \tag{3.4c}$$

where $f_{mxx}, g_{myx}, f_{mxy}, g_{myy}, f_{mxt}$ and g_{myt} can be obtained by Eq. (3.2b). Finally, all temporal derivatives of u_m can be obtained through the derivatives of flux f_m and g_m which are related to the spatial derivations of u_m . As a result, only the conserved variables u_m and their spatial gradients, e.g., $u_{mx}, u_{my}, u_{mxx}, u_{mxy}, u_{myx}$ and u_{myy} are the independent unknowns to be solved in the third-order CESE method. Once these seven variables are calculated, the flow solution structure inside the SE is completely determined.

3.3 Time-marching calculation of u_m

The solution of u_m can be obtained by integrating the second-order Taylor series expansion of the flow variables and the fluxes over CEs defined above. Here, the design of CE and SE is different from that in high-order CESE schemes in [23, 33]. Moreover, the integration is more complex than that in the original second-order CESE method because the flow variables and the fluxes are represented by the second-order Taylor series expansion. Below, we will illustrate the calculation of the flow variables u_m in third-order CESE method in detail.

In the generalized 3D Euclidean space $E_3(x,y,t)$, by using Gauss's divergence theorem, Eq. (2.1) can be rewritten as the following integral equations:

$$\oint_{S(V)} \mathbf{h}_m \cdot d\mathbf{s} = 0, \quad m = 1, 2, \dots, 8. \tag{3.5}$$

Here $\mathbf{h}_m = (u_m, f_m, g_m)$, $S(V)$ is the boundary of an arbitrary space-time region V in E_3 . And $\mathbf{h}_m \cdot d\mathbf{s}$ is the space-time flux \mathbf{h}_m leaving the region V through the surface element $d\mathbf{s}$, where $d\mathbf{s} = \mathbf{n}d\sigma$ with $d\sigma$ being the area of a surface element on $S(V)$, and \mathbf{n} is the outward unit normal to $d\mathbf{s}$.

Thus, by integrating Eq. (3.5) over the CCE, we obtain:

$$\sum_{\ell=1}^4 \iint_{top_\ell} u_m d\sigma = \sum_{\ell=1}^4 \iint_{bot_\ell} u_m d\sigma - \sum_{\ell=1}^4 \sum_{k=1}^2 \iint_{side_{k,\ell}} \mathbf{T}_m \cdot \mathbf{n} d\sigma, \quad m = 1, 2, \dots, 8, \tag{3.6}$$

where top_ℓ represents the four top surfaces of CEs: $A_1B_1QB_4$, $A_2B_2QB_1$, $A_3B_3QB_2$, and $A_4B_4QB_3$. bot_ℓ represents the four bottom surfaces of CEs: $A'_1B'_1Q'B'_4$, $A'_2B'_2Q'B'_1$, $A'_3B'_3Q'B'_2$, and $A'_4B'_4Q'B'_3$. $side_{k,\ell}$ represents the eight side faces of CEs: $A'_1B'_4B_4A_1$, $A'_1B'_1B_1A_1$, $A'_2B'_1B_1A_2$, $A'_2B'_2B_2A_2$, $A'_3B'_2B_2A_3$, $A'_3B'_3B_3A_3$, $A'_4B'_3B_3A_4$, and $A'_4B'_4B_4A_4$, respectively. $\mathbf{T}_m = (f_m, g_m)$ is the vector of the fluxes and \mathbf{n} is the unit outward normal vector of the corresponding surface. Similar to the original second-order CESE scheme, we integrate the second-order Taylor expansion of u_m , f_m and g_m , i.e., Eq. (3.1), to calculate u_m at the new step in the third-order CESE method. However, the integration in the third-order CESE method is more complex than that in the original second-order CESE method because u_m , f_m and g_m are represented by the second-order Taylor expansion in the third-order CESE method.

Firstly, we present the calculation of the flux through the four bottom surfaces of CEs. Take the bottom surface $A'_1B'_1Q'B'_4$ as an example, the flux through it is calculated based on the second-order Taylor expansion of the solutions stored at point $A_1'^*$ located at $(x_{A_1'^*}, y_{A_1'^*}, t^{n-1/2})$:

$$\iint_{A'_1B'_1Q'B'_4} u_m d\sigma = \iint_{A'_1B'_1Q'B'_4} \sum_{a=0}^2 \sum_{b=0}^{2-a} \frac{1}{a!b!} \frac{\partial^{a+b}(u_m)_{A_1'^*}}{\partial x^a \partial y^b} (x - x_{A_1'^*})^a (y - y_{A_1'^*})^b dx dy. \tag{3.7}$$

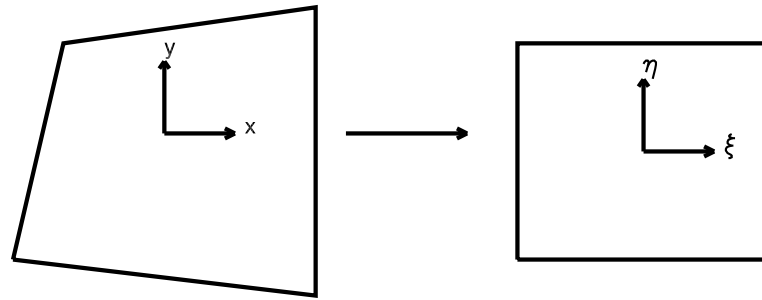


Figure 3: Schematic illustration of the coordinate transformation from physical to reference element.

For computational efficiency, we transform the quadrangle $A'_1B'_1Q'B'_4$ in the physical coordinates (x,y) into a right square in the computational domain (ξ,η) as illustrated in Fig. 3. Thereafter, the integration of the space-time flux u_m over quadrangle $A'_1B'_1Q'B'_4$, i.e., Eq. (3.7), can be calculated as follows:

$$\begin{aligned} & \iint_{A'_1B'_1Q'B'_4} u_m d\sigma \\ &= \frac{1}{a!b!} \frac{\partial^{a+b}(u_m)_{A'_1}}{\partial x^a \partial y^b} \int_{-1}^1 \int_{-1}^1 \sum_{a=0}^2 \sum_{b=0}^{2-a} (x(\xi,\eta) - x_{A'_1}(\xi,\eta))^a (y(\xi,\eta) - y_{A'_1}(\xi,\eta))^b |\det \mathbf{J}| d\xi d\eta, \end{aligned}$$

where \mathbf{J} is the coordinate transformation Jacobi matrix given by

$$\mathbf{J} = \frac{\partial(x,y)}{\partial(\xi,\eta)} = \begin{pmatrix} x_\xi & y_\xi \\ x_\eta & y_\eta \end{pmatrix} = \begin{pmatrix} \sum_{i=1}^4 x_i \frac{\partial N_i}{\partial \xi} & \sum_{i=1}^4 y_i \frac{\partial N_i}{\partial \xi} \\ \sum_{i=1}^4 x_i \frac{\partial N_i}{\partial \eta} & \sum_{i=1}^4 y_i \frac{\partial N_i}{\partial \eta} \end{pmatrix}.$$

Here, the transformation equation is given by

$$x = \sum_{i=1}^4 x_i N_i(\xi,\eta), \quad y = \sum_{i=1}^4 y_i N_i(\xi,\eta),$$

with shape functions

$$\begin{cases} N_1 = \frac{1}{4}(1-\xi)(1-\eta), & N_2 = \frac{1}{4}(1+\xi)(1-\eta), \\ N_3 = \frac{1}{4}(1+\xi)(1+\eta), & N_4 = \frac{1}{4}(1-\xi)(1+\eta). \end{cases}$$

Similarly, the fluxes through the other three bottom surfaces can be readily calculated at points A_2^*, A_3^*, A_4^* . The flux through the top surface can be calculated at Q^* , but it is an implicit function of the conserved variable u_m and its spatial derivatives stored at point Q^* . Moreover, the integration associated with the first-order derivatives of u_m over the

top surface of the CCE is null. Thus, the integration associated with $(u_m)_{Q^*}$ over the top surface of the CCE is

$$\begin{aligned} \sum_{\ell=1}^4 \iint_{top_\ell} u_m d\sigma &= (u_m)_{Q^*} Area_{oct} + \sum_{\ell=1}^4 \iint_{top_\ell} u_m^{II} d\sigma \\ &= (u_m)_{Q^*} Area_{oct} + \sum_{\ell=1}^4 \left(\sum_{a=0}^2 \sum_{b=0, a+b \geq 2}^{2-a} \frac{1}{a!b!} \frac{\partial^{a+b}(u_m)_{Q^*}}{\partial x^a \partial y^b} \right. \\ &\quad \left. \int_{-1}^1 \int_{-1}^1 (x(\xi, \eta) - x_{Q^*}(\xi, \eta))^a (y(\xi, \eta) - y_{Q^*}(\xi, \eta))^b |det \mathbf{J}_\ell| d\xi d\eta \right), \end{aligned}$$

where $Area_{oct}$ denotes the area of octagon $A_1 B_1 \dots A_4 B_4$, $\iint_{top_\ell} u_m^{II} d\sigma$ denotes the integration calculated by using the second-order derivatives of u_m stored at point Q^* .

Next, we present the calculation of the flux through the eight side surfaces of CEs. Take the side surface $A'_1 B'_1 B_1 A_1$ as an example, we illustrate the flux integration through the side surface in Eq. (3.6). The unit outward normal vector \mathbf{n} of the side surface $A'_1 B'_1 B_1 A_1$ is

$$\mathbf{n} = \frac{[(y_{B'_1} - y_{A'_1}), -(x_{B'_1} - x_{A'_1}), 0]}{\sqrt{(x_{B'_1} - x_{A'_1})^2 + (y_{B'_1} - y_{A'_1})^2}}.$$

Because the projection of the side face $A'_1 B'_1 B_1 A_1$ to the spatial domain is the line segment $\overline{A_1 B_1}$, we represent spatial displacement by a single parameter α . The differential area for the integration is $d\sigma = (\Delta t/2) \sqrt{(x_{B'_1} - x_{A'_1})^2 + (y_{B'_1} - y_{A'_1})^2} d\alpha d\beta$. Thus, we have

$$\iint_{A'_1 B'_1 B_1 A_1} \mathbf{T}_m \cdot \mathbf{n} d\sigma = \frac{\Delta t}{2} \int_0^1 \int_0^1 [(y_{B'_1} - y_{A'_1})(f_m) - (x_{B'_1} - x_{A'_1})(g_m)] d\alpha d\beta. \tag{3.8}$$

The value of T_m (f_m or g_m) on the side surface $A'_1 B'_1 B_1 A_1$ is expressed by the second-order space-time Taylor series expansion at point A_1^* as

$$T_m = \sum_{a=0}^2 \sum_{b=0}^{2-a} \sum_{c=0}^{2-a-b} \frac{1}{a!b!c!} \frac{\partial^{a+b+c}(T_m)_{A_1^*}}{\partial x^a \partial y^b \partial t^c} (x - x_{A_1^*})^a (y - y_{A_1^*})^b (t - t_{n-1/2})^c.$$

Similarly, the fluxes through the other side surfaces can be readily calculated based on the corresponding solution points in the previous time step.

Thus, the space-time flux through all surfaces of the CCE leads to an solution of $(u_m)_{Q^*}$

$$(u_m)_{Q^*} = \frac{-1}{Area_{oct}} \sum_{\ell=1}^4 \left[\iint_{top_\ell} u_m^{II} d\sigma - \iint_{bot_\ell} u_m d\sigma - \sum_{k=1}^2 \iint_{side_{k,\ell}} \mathbf{T}_m \cdot \mathbf{n} d\sigma \right]. \tag{3.9}$$

Here, the fluxes through the side and bottom surfaces of the CCE are calculated by using the known solutions at the previous time step associated with the four neighboring solution points, i.e., points $A_1^*, A_2^*, A_3^*, A_4^*$. The flux through the top surface of the CCE is calculated by using the solutions at point Q^* at the new time step. To calculate $\iint_{top} u_m^I d\sigma$, we need the new second-order derivatives at point Q^* . Therefore, the computational sequence is as follows:

- 1: updating the second – order derivatives;
- 2: updating the conservative variables;
- 3: updating the first – order derivatives.

4 Time-marching calculation for spatial derivatives

There exist second-order spatial derivatives of $(u_m)_{Q^*}$ in the flux through the top surface of CCE, so it is first necessary to obtain the second-order derivatives. Below, we illustrate the procedure to calculate the second-order spatial derivatives at the new time level by employing the central-difference method and the reweighing method, see [36] and [22].

We can obtain the second-order spatial derivatives by using the first-order Taylor series expansion to approximate the first-order spatial derivatives. For example, we can calculate one pair of $(u_{mxx})_{Q^*}^1$ and $(u_{mxy})_{Q^*}^1$ by using the two neighbor points A_1^* and A_2^* of Q^* . Using first-order Taylor series we can write

$$\begin{aligned} (u_{mx})_{A_1^*} &= (u_{mx})'_{Q^*} + (u_{mxx})_{Q^*} \delta x_1 + (u_{mxy})_{Q^*} \delta y_1, \\ (u_{mx})_{A_2^*} &= (u_{mx})'_{Q^*} + (u_{mxx})_{Q^*} \delta x_2 + (u_{mxy})_{Q^*} \delta y_2, \end{aligned} \tag{4.1}$$

where $\delta x_1 = x_{A_1^*} - x_{Q^*}$, $\delta y_1 = y_{A_1^*} - y_{Q^*}$, $\delta x_2 = x_{A_2^*} - x_{Q^*}$, and $\delta y_2 = y_{A_2^*} - y_{Q^*}$.

$(u_{mx})_{A_1^*}$ and $(u_{mx})_{A_2^*}$ are the values at the new time step, and they can be evaluated using the values at the previous time level:

$$\begin{aligned} (u_{mx})_{A_1^*} &= (u_{mx})_{A_1^*} + (u_{mxt})_{A_1^*} \Delta t / 2, \\ (u_{mx})_{A_2^*} &= (u_{mx})_{A_2^*} + (u_{mxt})_{A_2^*} \Delta t / 2. \end{aligned} \tag{4.2}$$

$(u_{mx})'_{Q^*}$ is the temporary value at the new time step, which can be evaluated by applying the original second-order CESE method to the second-order equations (3.4a), and treating the first-order derivative terms as the unknowns.

To proceed, Eq. (3.4a) can be cast into the following divergence-free equations:

$$\nabla \cdot \mathbf{h}_{mx} = 0, \tag{4.3}$$

where $\mathbf{h}_{mx} = (u_{mx}, f_{mx}, g_{mx})$ are the additional space-time flux vectors. Aided by the Gauss theorem in the three-dimensional space-time domain, the above differential equations are

recast into the following integral equations:

$$\oint_{S(V)} \mathbf{h}_{mx} \cdot d\mathbf{s} = 0. \tag{4.4}$$

Next, we apply the original second-order CESE method [36] to calculate the temporary value $(u_{mx})_{Q^*}^1$ by imposing space-time flux conservation of h_{mx} .

Then, by using Cramer’s rule, we can obtain $(u_{mxx})_{Q^*}^1$ and $(u_{mxy})_{Q^*}^1$ at point Q^*

$$(u_{mxx})_{Q^*}^1 = \frac{\Delta_x}{\Delta}, \quad (u_{mxy})_{Q^*}^1 = \frac{\Delta_y}{\Delta}, \tag{4.5}$$

where

$$\Delta = \begin{vmatrix} \delta x_1 & \delta y_1 \\ \delta x_2 & \delta y_2 \end{vmatrix}, \quad \Delta_x = \begin{vmatrix} \delta u_m^1 & \delta y_1 \\ \delta u_m^2 & \delta y_2 \end{vmatrix}, \quad \Delta_y = \begin{vmatrix} \delta x_1 & \delta u_m^1 \\ \delta x_2 & \delta u_m^2 \end{vmatrix},$$

and $\delta u_m^1 = (u_{mx})_{A_1^*} - (u_{mx})'_{Q^*}$, $\delta u_m^2 = (u_{mx})_{A_2^*} - (u_{mx})'_{Q^*}$. In a similar manner, by using the first-order derivatives at the two neighbor points of Q^* , i.e., A_2^*, A_3^* , and $(u_{mx})'_{Q^*}$, we can get $(u_{mxx})_{Q^*}^2$ and $(u_{mxy})_{Q^*}^2$. By using the first-order derivatives at A_3^*, A_4^* and $(u_{mx})'_{Q^*}$, we get $(u_{mxx})_{Q^*}^3$ and $(u_{mxy})_{Q^*}^3$. By using the first-order derivatives at A_4^*, A_1^* and $(u_{mx})'_{Q^*}$, we get $(u_{mxx})_{Q^*}^4$ and $(u_{mxy})_{Q^*}^4$.

By a simple weighted average method, we calculate $(u_{mxx})_{Q^*}$ and $(u_{mxy})_{Q^*}$ at Q^*

$$(u_{mxx})_{Q^*} = \begin{cases} 0, & \text{if } \theta_{mk} = 0, \quad k = 1, 2, \dots, 4, \\ \sum_{k=1}^4 [(W_m^k)^\alpha (u_{mxx})_{Q^*}^k] / \sum_{k=1}^4 (W_m^k)^\alpha, & \text{otherwise,} \end{cases} \tag{4.6a}$$

$$(u_{mxy})_{Q^*} = \begin{cases} 0, & \text{if } \theta_{mk} = 0, \quad k = 1, 2, \dots, 4, \\ \sum_{k=1}^4 [(W_m^k)^\alpha (u_{mxy})_{Q^*}^k] / \sum_{k=1}^4 (W_m^k)^\alpha, & \text{otherwise,} \end{cases} \tag{4.6b}$$

where

$$W_m^k = \prod_{\ell=1, \ell \neq k}^4 \theta_{m\ell}, \quad \theta_{m\ell} = \sqrt{(u_{mxx}^\ell)^2 + (u_{mxy}^\ell)^2}.$$

α is an adjustable parameter that can control the viscosity of the scheme, and it is usually $= 0, 1, 2$. To avoid dividing by zero, in practice a small positive number such as 10^{-60} is added to the denominators that appear in Eqs. (4.6a) and (4.6b). Similarly, the second-order derivatives $(u_{myx})_{Q^*}$ and $(u_{myy})_{Q^*}$ at the new step are readily calculated. The method of calculating the second-order spatial derivatives is slightly different from that in [23] and [4]. It can be extended to calculate any even-order spatial derivatives.

Once the second-order spatial derivatives of $(u_m)_{Q^*}$ have all been calculated, $(u_m)_{Q^*}$ can be determined by Eq. (3.9). Then the first-order derivatives are also obtained by the

same central-difference method. But the first-order derivatives are obtained from the values of conservative variables at points $A_1^*, A_2^*, A_3^*, A_4^*$ approximated by the second-order Taylor expansion from the point Q^* .

$$(u_m)_{A_\ell^*} = (u_m)_{Q^*} + (u_{mx})_{Q^*} \delta x_\ell + (u_{my})_{Q^*} \delta y_\ell + \frac{1}{2} [(u_{mxx})_{Q^*} (\delta x_\ell)^2 + (u_{myy})_{Q^*} (\delta y_\ell)^2 + ((u_{mxy})_{Q^*} + (u_{myx})_{Q^*}) \delta x_\ell \delta y_\ell], \tag{4.7}$$

where $\ell = 1, 2, 3, 4$. $(u_m)_{A_\ell^*}$ can be evaluated from the preceding half time level

$$(u_m)_{A_\ell^*} = (u_m)_{A_\ell^{*'}} + \frac{\Delta t}{2} (u_{mt})_{A_\ell^{*'}} + \frac{1}{2} (u_{mtt})_{A_\ell^{*'}} \left(\frac{\Delta t}{2} \right)^2.$$

Thus, the first-order derivatives $(u_{mx})_{Q^*}$ and $(u_{my})_{Q^*}$ can be readily determined by the central-difference method described above.

However, the high-order numerical schemes easily produce spurious oscillations near discontinuities, which may, indeed, lead to numerical instabilities. Here, in order to further eliminate oscillations near discontinuities and preserve the high-order accuracy in smooth regions simultaneously, limiting would only be used near discontinuities which is detected by the discontinuity detection scheme. Krivodonova *et al.* [18] found that limiting only where suggested by detection strategy preserved a high order of accuracy in regions where solutions were smooth.

Similar to that of [38], a simple discontinuity detection method is used to detect the ‘trouble cells’ in discontinuity region. For convenience, we take notations $[q]^1$ and \bar{q}^1 as the jump and mean values at the interface $B_1' B_4' B_4 B_1$.

$$[q]^1 = |q_r^1 - q_l^1|, \quad \bar{q}^1 = \frac{|q_r^1 + q_l^1|}{2},$$

where q_l^1 and q_r^1 are the variables on the left and the right sides of the interface $B_1' B_4' B_4 B_1$. We compute the left value q_l^1 from point A_1^* and the right value q_r^1 from point Q^* using the second-order Taylor expansion

$$\begin{aligned} q_l^1 &= q_{A_1^*} + (q_x)_{A_1^*} \Delta x_{A_1^*}^1 + (q_y)_{A_1^*} \Delta y_{A_1^*}^1 + (q_t)_{A_1^*} \Delta t_{A_1^*} + \frac{1}{2} \left\{ (q_{xx})_{A_1^*} (\Delta x_{A_1^*}^1)^2 \right. \\ &\quad \left. + (q_{yy})_{A_1^*} (\Delta y_{A_1^*}^1)^2 + (q_{tt})_{A_1^*} (\Delta t_{A_1^*})^2 + [(q_{xy})_{A_1^*} + (q_{yx})_{A_1^*}] \Delta x_{A_1^*}^1 \Delta y_{A_1^*}^1 \right\} \\ &\quad + (q_{xt})_{A_1^*} \Delta x_{A_1^*}^1 \Delta t_{A_1^*} + (q_{yt})_{A_1^*} \Delta y_{A_1^*}^1 \Delta t_{A_1^*}, \\ q_r^1 &= q_{Q^*} + (q_x)_{Q^*} \Delta x_{Q^*}^1 + (q_y)_{Q^*} \Delta y_{Q^*}^1 + (q_t)_{Q^*} \Delta t_{Q^*} + \frac{1}{2} \left\{ (q_{xx})_{Q^*} (\Delta x_{Q^*}^1)^2 \right. \\ &\quad \left. + (q_{yy})_{Q^*} (\Delta y_{Q^*}^1)^2 + (q_{tt})_{Q^*} (\Delta t_{Q^*})^2 + [(q_{xy})_{Q^*} + (q_{yx})_{Q^*}] \Delta x_{Q^*}^1 \Delta y_{Q^*}^1 \right\} \\ &\quad + (q_{xt})_{Q^*} \Delta x_{Q^*}^1 \Delta t_{Q^*} + (q_{yt})_{Q^*} \Delta y_{Q^*}^1 \Delta t_{Q^*}, \end{aligned}$$

where $\Delta x_{A_1^*}^1 = x^1 - x_{A_1^*}$, $\Delta y_{A_1^*}^1 = y^1 - y_{A_1^*}$, $\Delta t_{A_1^*} = t - t^{n-1/2}$, $\Delta x_{Q^*}^1 = x^1 - x_{Q^*}$, $\Delta y_{Q^*}^1 = y^1 - y_{Q^*}$, and $\Delta t_{Q^*} = t - t^{n-1}$. (x^1, y^1) is the centroid of the interface $B_1' B_4' B_4 B_1$. Similarly for those at the other three interfaces: $B_1' B_2' B_2 B_1$, $B_2' B_3' B_3 B_2$, and $B_3' B_4' B_4 B_3$, we can obtain $[q]^2, \bar{q}^2, [q]^3, \bar{q}^3, [q]^4, \bar{q}^4$. Then we can define shock indicator D_{Q^*} for point Q^*

$$D_{Q^*} = \frac{1}{h^{1+1/2}} \max \left[\left| \frac{[q]^1}{\bar{q}^1} \right|, \left| \frac{[q]^2}{\bar{q}^2} \right|, \left| \frac{[q]^3}{\bar{q}^3} \right|, \left| \frac{[q]^4}{\bar{q}^4} \right| \right],$$

where h is the length of the grid, q is a solution component or a derived quantity from a solution component (e.g., a characteristic variables, the density, or the entropy). In this paper, the density is appointed as the detection variable. If $D_{Q^*} > \theta$, point Q^* is a trouble cell. Where θ is the indicator parameter, and we let $\theta = 0.5$.

For ‘trouble cells’, we use the widespread minmod function to limit the spatial derivatives [28]. The minmod function is defined as

$$\text{minmod}(w_1, w_2, \dots, w_n) = \text{sgn}(w_1) \max[0, \min(|w_1|, \text{sgn}(w_1)w_2, \dots, \text{sgn}(w_1)w_n)].$$

Take $(u_{mxx})_{Q^*}$ as an example, we limit it as

$$(u_{mxx})_{Q^*} = \text{minmod} \left((u_{mxx})_{Q^*}^1, (u_{mxx})_{Q^*}^2, (u_{mxx})_{Q^*}^3, (u_{mxx})_{Q^*}^4 \right).$$

Similarly, the other spatial derivatives are limited.

A critical issue in computational MHD is to maintain the divergence-free condition for the magnetic field. In order to keep the divergence-free condition for magnetic fields, the same method of divergence-free in [33] is applied. In the following, we will briefly illustrate the method for divergence-free magnetic field.

By combining Eq. (4.7) relative to conservative variables u_6 and u_7 at the four neighbor points $A_1^*, A_2^*, A_3^*, A_4^*$ with the magnetic field divergence-free condition $\nabla \cdot \mathbf{B} = u_{6x} + u_{7y} = 0$, we can obtain a overdetermined equations

$$AX = C, \tag{4.8}$$

where

$$A = \begin{bmatrix} \delta x_1 & \delta y_1 & 0 & 0 \\ \delta x_2 & \delta y_2 & 0 & 0 \\ \delta x_3 & \delta y_3 & 0 & 0 \\ \delta x_4 & \delta y_4 & 0 & 0 \\ 0 & 0 & \delta x_1 & \delta y_1 \\ 0 & 0 & \delta x_2 & \delta y_2 \\ 0 & 0 & \delta x_3 & \delta y_3 \\ 0 & 0 & \delta x_4 & \delta y_4 \\ 1 & 0 & 0 & 1 \end{bmatrix}, \quad X = \begin{bmatrix} (u_{6x})_{Q^*} \\ (u_{6y})_{Q^*} \\ (u_{7x})_{Q^*} \\ (u_{7y})_{Q^*} \end{bmatrix}, \quad C = \begin{bmatrix} \delta u_6^1 \\ \delta u_6^2 \\ \delta u_6^3 \\ \delta u_6^4 \\ \delta u_7^1 \\ \delta u_7^2 \\ \delta u_7^3 \\ \delta u_7^4 \\ 0 \end{bmatrix}.$$

The number of equations is greater than the number of unknowns. Then, by using the least-squares method, we can obtain the first-order derivatives $(u_{6x})_{Q^*}, (u_{6y})_{Q^*}, (u_{7x})_{Q^*}, (u_{7y})_{Q^*}$. The other derivatives are still obtained using the central-difference method previously presented in Eqs. (4.5), (4.6a) and (4.6b).

5 Numerical examples

To assess the accuracy of the third-order CESE method and test its validity in simulating 2D MHD problems, we study the following benchmark problems. We choose the adjustable constant $\alpha=0$ for the first example and $\alpha=2$ for the other examples in Eqs. (4.6a) and (4.6b).

5.1 Smooth Alfvén wave problem

We first solve the smooth Alfvén wave problem [29] to check the accuracy of our scheme. The Alfvén wave propagates at an angle of $\theta=45^\circ$ with respect to the x -axis in the domain $[0,1/\cos\theta] \times [0,1/\sin\theta]$. The initial conditions are taken as

$$\begin{aligned} \rho &= 1, v_{\parallel} = 0, \quad v_{\perp} = 0.1 \sin(2\pi x_1), \quad v_z = 0.1 \cos(2\pi x_1), \\ p &= 0.1, \quad B_{\parallel} = 1, \quad B_{\perp} = v_{\perp}, \quad B_z = v_z, \end{aligned}$$

where $x_1 = x \cos(\theta) + y \sin(\theta)$. The adiabatic index is $\gamma = 5/3$. In this problem, the Alfvén wave propagates periodically towards the origin with a constant Alfvén wave speed $B_{\perp} / \sqrt{\rho} = 1$ and returns to its initial state whenever t becomes an integer. The Alfvén wave is a traveling wave. Note that the wave becomes standing if $v_{\parallel} = 1$.

We rotate the coordinates with the propagation angle θ and let the new coordinates be (ζ, η) . The initial conditions of vector variables in $x-y$ coordinate are obtained by coordinate transformation as:

$$\begin{aligned} \zeta_x &= \zeta_{\parallel} \cos(\theta) - \zeta_{\perp} \sin(\theta), \\ \zeta_y &= \zeta_{\parallel} \sin(\theta) + \zeta_{\perp} \cos(\theta) \quad (\zeta = v \text{ or } B). \end{aligned} \tag{5.1}$$

The problem is solved on $N \times N$ meshes with $N = 16, 32, 64, 128$. Periodic boundary conditions are imposed in both the x and y directions. The simulation is run to a final time $t = 2$ with a time step $\Delta t = 0.4/N$. We estimate the relative numerical error of any fluid variable v by

$$\delta_N(v) = \frac{\sum_{j=1}^N \sum_{k=1}^N |v_{j,k}^N - v_{j,k}^{exact}|}{N \times N}.$$

That average numerical errors are defined by $\delta_N = \frac{1}{4}(\delta_N(v_{\perp}) + \delta_N(v_z) + \delta_N(B_{\perp}) + \delta_N(B_z))$. The corresponding convergence rate is computed as: $R_N = \log(\delta_{N_1} / \delta_{N_2}) / \log(N_2 / N_1)$. Table 1 gives the average numerical errors and convergence rates of accuracy obtained by the third-order CESE scheme for the traveling wave problem and the standing wave problem. The results show that the method converges approximately at a third order rate for smooth solutions.

Table 1: Numerical errors (δ_N) and convergence order (R_N) for the smooth Alfvén wave problem at $t=2$.

N	Traveling waves		Standing waves	
	δ_N	R_N	δ_N	R_N
16	3.5950E-3	-	5.1254E-3	-
32	4.4749E-4	3.0061	6.3753E-4	3.0071
64	5.5705E-5	3.0060	7.9119E-5	3.0104
128	6.9554E-6	3.0016	9.8659E-6	3.0035

5.2 Brio-Wu shock tube problem

This shock tube problem is originally from [5], which is a classical test problem for ideal MHD codes [17, 29]. The initial left and right states of this one-dimensional Riemann problem are

$$(\rho, v_{||}, v_{\perp}, v_z, p, B_{||}, B_{\perp}, B_z) = \begin{cases} (1.000, 0, 0, 0, 1.0, 0.75, 1.0, 0), & \text{left,} \\ (0.125, 0, 0, 0, 0.1, 0.75, -1.0, 0), & \text{right,} \end{cases}$$

with $\gamma=2$, where $||$ refers to the direction along the normal of the shock front, \perp refers to the direction perpendicular to the normal of the shock front. Through a simple coordinate transformation, Eq. (5.1), the initial profiles of velocity and magnetic fields in the $x-y$ coordinates are obtained. We solve it as a fully 2-D problem with an angle $\theta=45^\circ$ between the shock interface and y -axes. The computational domain is $[0, \sqrt{2}/2] \times [0, \sqrt{2}/2]$.

Fig. 4 shows the comparison between one-dimensional reference results and two-dimensional results from the second- and third-order CESE schemes at $t=0.1$. One-dimensional results computed with 2000 grid cells are plotted by black lines. The red and blue lines represent the results of the third-order scheme and the second-order scheme, respectively. We can see that the third-order results are in favorable agreement with the one-dimensional ones. The results of the third-order CESE scheme are superior than those of the second-order CESE scheme. However, we can see a little oscillation in the results of the third-order scheme, which is similar to the result of the third-order CESE scheme in [23] for shock tube problem of Euler.

5.3 Orszag-Tang vortex

The Orszag-Tang vortex problem [21] has been used in many papers, e.g., [11, 16, 19, 37] as a two-dimensional numerical test for MHD codes. The computational domain is a square $[0, 2\pi] \times [0, 2\pi]$ with periodic boundary conditions on boundaries in both x - and y directions. The initial conditions of the flow field are:

$$\begin{aligned} \rho &= \gamma^2, & p &= \gamma, & u &= -\sin(y), & v &= \sin(x), & w &= 0, \\ B_x &= -\sin(y), & B_y &= \sin(2x), & B_z &= 0. \end{aligned}$$

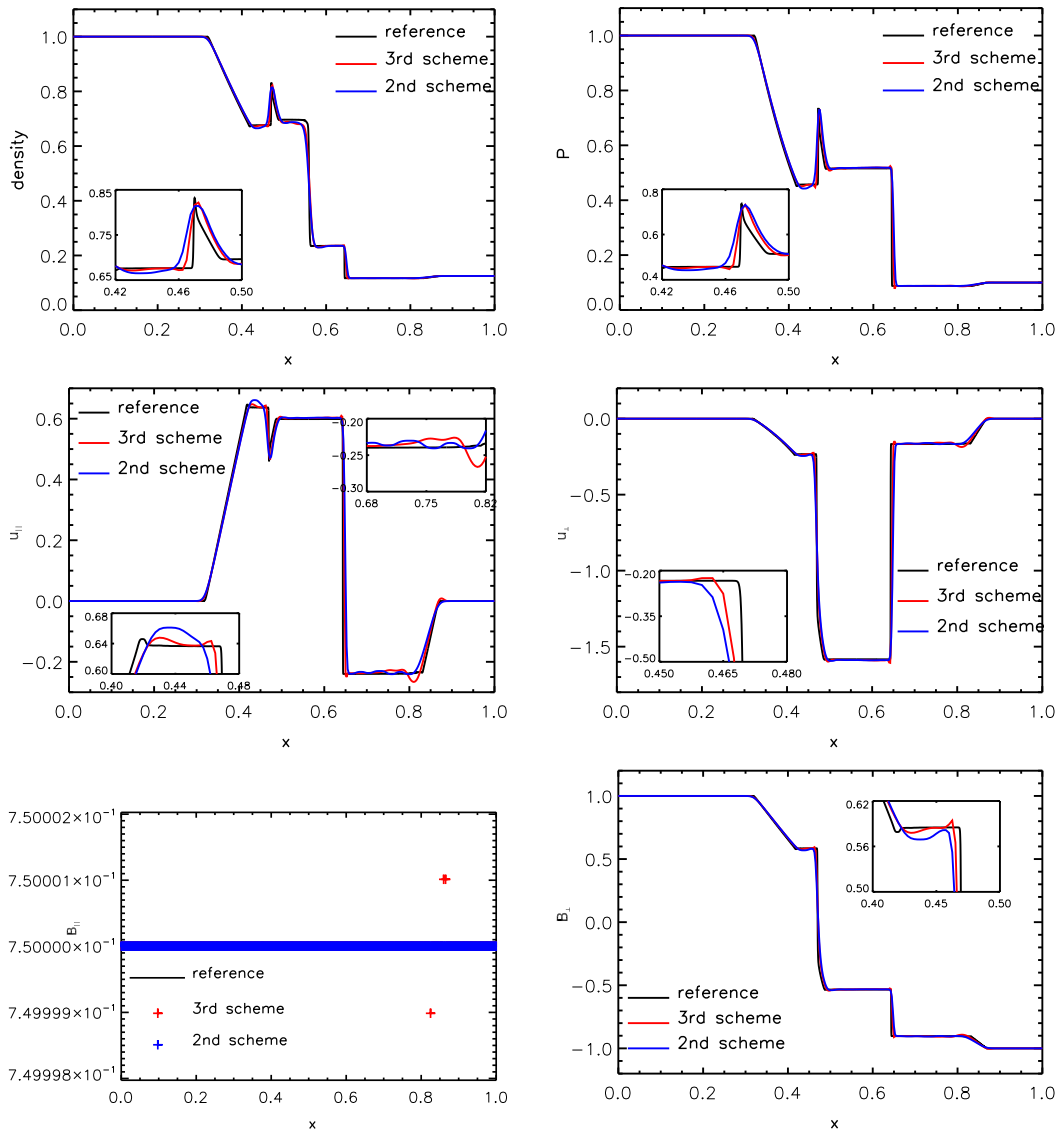


Figure 4: The solutions for the Briou-Wu shock tube problem on a 400×400 grid. The reference solution is computed with 2000 grid cells in 1D problem.

The Orszag-Tang vortex problem starts from smooth initial data, but gradually the flow becomes very complex as expected from a transition towards turbulence. Fig. 5 shows the pressure contours of the third-order CESE results on a 400×400 grid at time $t=0.5, 2$ and 3 , respectively. From the results, we can see that there is no obvious difference between the present results and those in previous papers [16,37]. For quantitative details of the calculated results, Fig. 6 shows the pressure profiles along the line of $y = 0.625\pi$

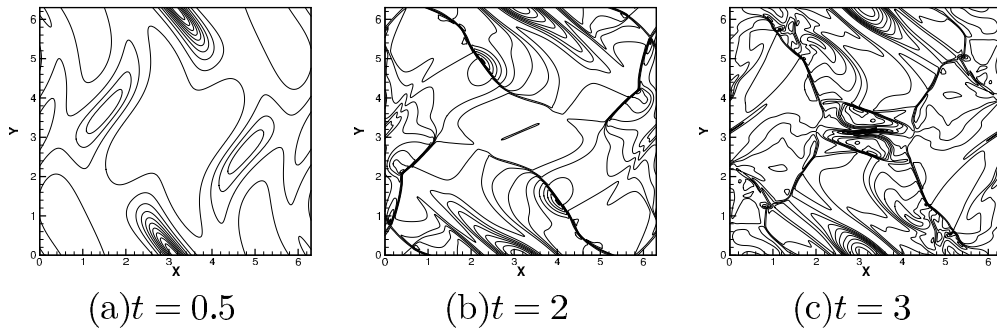


Figure 5: The contour plots of pressure for the vortex problem with 400×400 grids at (a) $t=0.5$, (b) $t=2$, and (c) $t=3$, respectively. 12 contour levels range from 1.0 to 5.8 for $t=0.5$, from 0.14 to 6.9 for $t=2$, and from 0.36 to 6.3 for $t=3$, respectively.

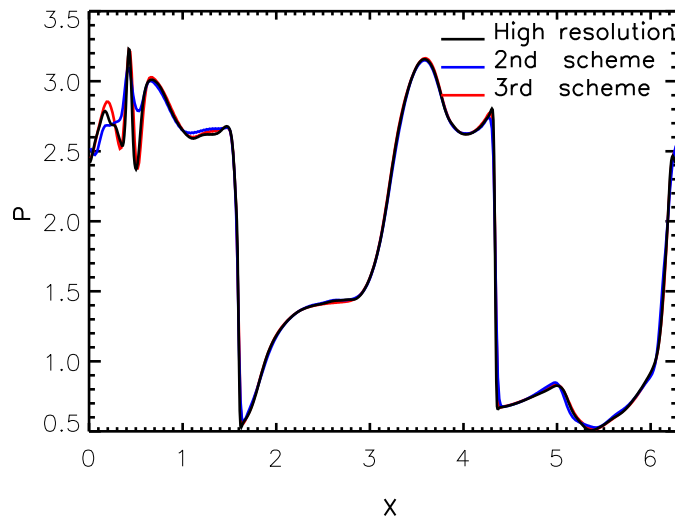


Figure 6: Pressure profiles of the vortex problem along line $y=0.625\pi$ on a 400×400 grid at $t=3$. The reference high resolution solution is computed with 800×800 grids using the original second-order CESE scheme.

at time $t=3$. The results from the second- and third-order schemes are compared to the high resolution solution. The black line represents the reference high resolution solution obtained with the original second-order CESE scheme on an 800×800 grid. From the results, it can be seen that the third-order scheme yields a better resolution than the second-order scheme, and the third-order scheme can indeed enhance the accuracy of the solution. It can also be seen that the third-order result has similar quality as compared to the second-order result by using four times meshes.

5.4 Rotor problem

This problem was considered in [1, 2, 12, 29]. We use exactly the same set-up of the problem as was described in [29]. The problem consists of having a dense, rapidly spinning cylinder, in the center of a static, magnetized background with uniform pressure. The initial fluid are

$$(\rho, v_x, v_y) = \begin{cases} (10, -v_0(y-0.5)/r_0, v_0(x-0.5)/r_0), & r < 0.1, \\ (1+9f, -fv_0(y-0.5)/r, fv_0(x-0.5)/r), & 0.1 \leq r \leq 0.115, \\ (1, 0, 0), & r > 0.115, \end{cases}$$

with $p = 1, B_x = 5/\sqrt{4\pi}$ and adiabatic index $\gamma = 1.4$, where $v_0 = 2$, $r = [(x-0.5)^2 + (y-0.5)^2]^{1/2}$, and $f = (23 - 200r)/3$ is a linear taper, which is applied to linearly join the density in the ambient. The rotor is not in equilibrium, since the centrifugal forces are not balanced.

The computational domain is a square $[0, 1] \times [0, 1]$ with outflow boundary conditions on all four sides. Fig. 7 shows the density, pressure, Mach number, and the magnitude of the magnetic field, respectively, on a uniform 400×400 grid at time $t = 0.15$. These results are in good agreement with the computations in [1, 2, 29], thereby showing that the method presented in this paper is indeed very valuable for numerical MHD.

6 Conclusion

In this paper, we propose a third-order CESE method to simulate 2D MHD equations. The ideas and treatments of the third-order CESE method are kept the same with those of the original second-order CESE method. A second-order Taylor series in space and time is used to discretize the unknowns and the fluxes inside each SE. Space and time are treated in a unified manner in discretization. The present scheme preserve the beauty of local and global conservativeness of the original CESE method. The flux at the cell interface can be calculated directly without using an approximated Riemann solver. Moreover, the method only involve the immediate neighboring mesh cells of the solution point.

In order to check the accuracy of the scheme, we solve the smooth Alfvén wave problem. The result shows that the method converges approximately at a third order rate for smooth solutions. Then, to demonstrate the capabilities of the CESE method for MHD problems, we simulate three 2D MHD benchmark problems, such as oblique shock tube problem, Orszag-Tang vortex and rotor problem, and compare the results to those of the original second-order CESE method. The results show that the third-order scheme described in this paper have higher numerical accuracy than the second-order scheme. The third-order CESE method is very easily straightforward extended to any odd-order CESE method. Moreover, it can also be easily extended to three-dimensional scheme on 3D unstructured meshes. In the future work, we will construct the 3D third-order CESE

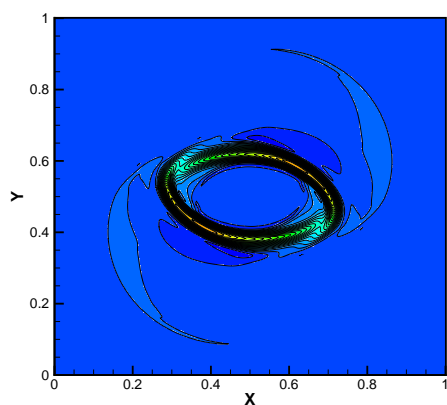
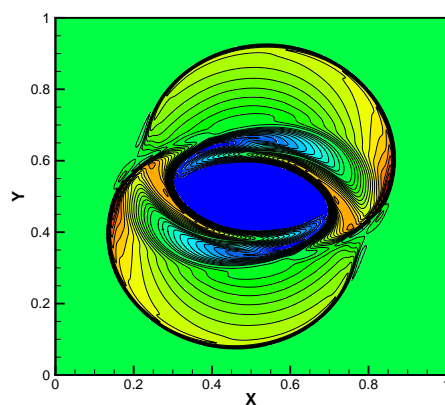
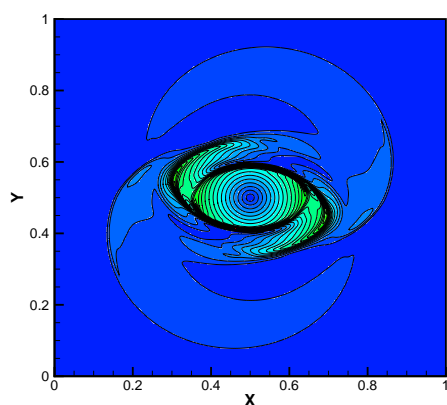
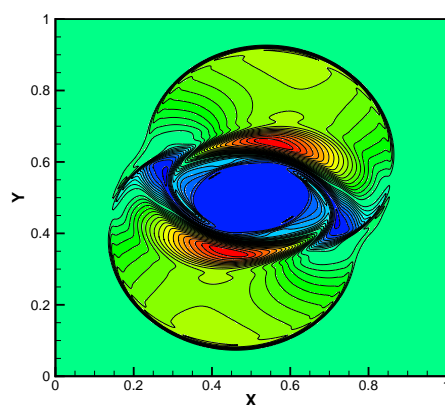
(a) ρ (b) p (c) $|v|/C_s$ (d) $B^2/2$

Figure 7: The density, thermal pressure, Mach number, and magnetic pressure at $t=0.15$ for the rotor problem on a 400×400 grid. The 30 contour lines are shown for the ranges $0.483 < \rho < 12.95$, $0.0202 < p < 2.008$, $0 < |v|/c_s < 8.18$, and $0.0787 < B^2/2 < 2.5315$, respectively.

method and apply it to simulate solar wind background and disturbance propagation in the corona and in interplanetary space and other astrophysical MHD flow problems.

Acknowledgments

This research is jointly supported by the National Natural Science Foundation of China (Grant Nos. 42030204, 41874202), Shenzhen Natural Science Fund (the Stable Support Plan Program GXWD20220817152453003), Shenzhen Key Laboratory Launching Project (No. ZDSYS20210702140800001) and the Specialized Research Fund for State Key Labo-

ratories. The work was carried out on TianHe-1(A) for National Supercomputer Center in Tianjin, China.

References

- [1] D. S. Balsara, D. Spicer, A staggered mesh algorithm using high order Godunov fluxes to ensure solenoidal magnetic fields in magnetohydrodynamic simulations, *J. Comput. Phys.*, 149 (1999), 270-292.
- [2] D. S. Balsara, Second-order-accurate schemes for magnetohydrodynamics with divergence-free reconstruction, *The Astrophysical Journal Supplement Series*, 151 (2004), 149-184.
- [3] D. L. Bilyeu, Y.-Y. Chen, S.-T. J. Yu, High-order CESE methods for the Euler equations, in: 49th AIAA Aerospace Sciences Meeting, AIAA Paper 2011-1065 (2011).
- [4] D. L. Bilyeu and S.-T. J. Yu and Y.-Y. Chen and J.-L. Cambier, A two-dimensional fourth-order unstructured-meshed Euler solver based on the CESE method, *J. Comput. Phys.*, 257 (2014), 981-999.
- [5] M. Brio, C. C. Wu, An upwinding differencing schemes for the equations for ideal magnetohydrodynamics, *J. Comput. Phys.*, 75 (1988), 400.
- [6] S. C. Chang, The method of space-time conservation element and solution element – A new approach for solving the Navier-Stokes and Euler equations, *J. Comput. Phys.*, 119 (1995), 295-324.
- [7] S. C. Chang, X. Y. Wang, C. Y. Chow, The space-time conservation element and solution element method: A new high resolution and genuinely multidimensional paradigm for solving conservation laws, *J. Comput. Phys.*, 156 (1999), 89-136.
- [8] S. C. Chang, X. Y. Wang, Multi-dimensional Courant number insensitive CE/SE Euler solvers for application involving highly non-uniform meshes, AIAA Paper 2003-5285 (2003).
- [9] S. C. Chang, A new approach for constructing highly stable high order CESE schemes, in: 48th AIAA Aerospace Science Meeting, AIAA Paper 2010-543 (2010).
- [10] C. L. Chang, Time-accurate, unstructured-mesh Navier-Stokes computations with the space-time CESE method, 42nd AIAA/ ASME/SAE/ASEE Joint Propulsion Conference and Exhibit, AIAA Paper 2006-4780 (2006).
- [11] A. J. Christlieb, X. Feng, D. C. Seal, Q. Tang, A high-order positivity-preserving single-stage single-step method for the ideal magnetohydrodynamic equations. *J. Comput. Phys.*, 316 (2016), 218-242.
- [12] A. J. Christlieb, X. Feng, Y. Jiang, Q. Tang, A high-order finite difference WENO scheme for ideal magnetohydrodynamics on curvilinear meshes. *SIAM Journal on Scientific Computing*, 40.4 (2018), A2631-A2666.
- [13] X. S. Feng, L. P. Yang, C. Q. Xiang, et al., Three-dimensional solar wind modeling from the Sun to Earth by a SIP-CESE MHD model with a six-component grid, *Astrophys. J.*, 723 (2010), 300-319.
- [14] X. S. Feng, Y. F. Zhou, S. T. Wu, A novel numerical implementation for solar wind modeling by the modified conservation element/solution element method, *Astrophys. J.*, 655 (2007), 1110-1126.
- [15] Y. Guo, Hsu, A. T. Wu, J., Yang, Z., and A. Oyediran, Extension of CE/SE method to 2-D viscous flows, *Computers and Fluids*, 33 (2004), 1349-1361.
- [16] G. S. Jiang, C.C. Wu, A high-order WENO finite difference scheme for the equations of ideal magneto-hydrodynamics, *J. Comput. Phys.*, 150 (1999), 561-594.

- [17] F. Kanbar, R. Touma, C. Klingenberg, Well-balanced central scheme for the system of MHD equations with gravitational source term, *Commun. Comput. Phys.*, 32 (2022), 878-898.
- [18] L. Krivodonova, J. Xin, J. F. Remacle, N. Chevaugeon, J. E. Flaherty, Shock detection and limiting with discontinuous Galerkin methods for hyperbolic conservation laws, *Appl. Numer. Math.* 48 (2004) 323-338.
- [19] S. T. Li, High order central scheme on overlapping cells for magneto-hydrodynamic flows with and without constrained transport method, *J. Comput. Phys.*, 227 (2008), 7368-7393.
- [20] K. X. Liu, J. T. Wang, Analysis of high accuracy conservation element and solution element schemes, *Chin. Phys. Lett.*, 21 (2004), 2085-2088.
- [21] A. Orszag and C. M. Tang, Small-scale structure of two-dimensional magnetohydrodynamic turbulence, *J. Fluid Mech.*, 90 (1979), 129.
- [22] S. Qamar, S. Mudasser, On the application of a variant CE/SE method for solving two-dimensional ideal MHD equations, *Applied Numerical Mathematics*, 60 (2010), 587-606.
- [23] H. Shen, C. Y. Wen, K. X. Liu, Robust high-order space-time conservative schemes for solving conservation on hybrid Meshes, *J. Comput. Phys.*, 281 (2015), 375-402.
- [24] H. Shen, C.-Y. Wen, and D.-L. Zhang, A characteristic space-time conservation element and solution element method for conservation laws, *J. Comput. Phys.*, 288 (2015), 101-118.
- [25] H. Shen, and C.-Y. Wen, A characteristic space-time conservation element and solution element method for conservation laws II. Multidimensional extension, *J. Comput. Phys.*, 305 (2016), 775-792.
- [26] H. Shen, C.-Y. Wen, M. Parsani, and C.-W. Shu, Maximum-principle-satisfying space-time conservation element and solution element scheme applied to compressible mult fluids, *J. Comput. Phys.*, 330 (2017), 668-692.
- [27] H. Shen, and M. Parsani, Positivity-preserving CESE schemes for solving the compressible Euler and Navier-Stokes equations on hybrid unstructured meshes, *Computer Physics Communications*, 232 (2018), 165-176.
- [28] G. Toth, and D. Odstrcil, Comparison of some flux corrected transport and total variation diminishing numerical schemes for hydrodynamic and magnetohydrodynamic problems, *J. Comput. Phys.*, 128 (1996), 82-100.
- [29] G. Toth, The $\nabla \cdot B = 0$ constraint in shock-capturing magnetohydrodynamics codes, *J. Comput. Phys.*, 161 (2000), 605-652.
- [30] B. S. Venkatachari, G. C. Cheng, B. K. Soni, S. C. Chang, Validation and verification of Courant number insensitive CE/SE method for transient viscous flow simulations, *Mathematics and Computers in Simulation*, 78 (2008), 653-670.
- [31] J. T. Wang, K. X. Liu, D. L. Zhang, A new CE/SE scheme for multi-material elastic-plastic flow and its application, *Comput. Fluids* 38 (2009), 544-551.
- [32] K. W. Wu, D. B. Xiu, X. H. Zhong, A WENO-based stochastic galerkin scheme for ideal MHD equations with random inputs, *Commun. Comput. Phys.*, 30 (2021), 423-447.
- [33] Y. Yang, X. S. Feng, and C. W. Jiang, A high-order CESE scheme with a new divergence-free method for MHD numerical simulation, *J. Comput. Phys.*, 349 (2017), 561-581.
- [34] J. C. Yen and D. A. Wagner, Computational aeroacoustics using a simplified Courant number insensitive CE/SE method, *AIAA Paper 2005-2820* (2005).
- [35] J. C. Yen and E. G. Duell, W. Martindale, Computational aeroacoustics using 3D CESE method with a simplified Courant number insensitive scheme, *AIAA Paper 2006-2417* (2006).
- [36] M. Zhang, S. T. Yu, S. C. Chang, A space-time conservation element and solution element method for solving the two- and three-dimensional unsteady Euler equations using quadri-

- lateral and hexahedral meshes, *J. Comput. Phys.*, 175 (2002), 168-199.
- [37] M. Zhang, S. T. John Yu, S.-C. Henry Lin, S.-C. Chang, I. Blankson, Solving the MHD equations by the space-time conservation element and solution element method, *J. Comput. Phys.*, 214 (2006), 599-617.
- [38] L. P. Zhang, W. Liu, L. X. He, X. G. Deng, H. X. Zhang, A class of hybrid DG/FV methods for conservation laws I: Basic formulation and one-dimensional systems, *J. Comput. Phys.*, 231 (2012), 1081-1103.